Manufacture-friendly nanostructured metals stabilized by dual-phase honeycomb shell

Hai Wang
Shi-changxu Innovation Center for Advanced Materials, Institute of Metal Research, Chinese Academy of Sciences
Wei Song
School of Materials Science and Engineering, University of Science and Technology of China
Mingfeng Liu
Institute of Metal Research, Chinese Academy of Sciences
Shuyuan Zhang
School of Materials Science and Engineering, University of Science and Technology of China
Ling Ren (lren@imr.ac.cn)
Institute of Metal Research, Chinese Academy of Sciences
Dong Qiu
RMIT University https://orcid.org/0000-0003-4978-2077
Xing-Qiu Chen
Institute of Metal Research, Chinese Academy of Sciences https://orcid.org/0000-0002-5904-6578
Ke Yang
Institute of Metal Research

Article

Keywords: metallic materials, nanoscale refinement, honeycomb shell

Posted Date: June 2nd, 2021

DOI: https://doi.org/10.21203/rs.3.rs-551013/v1

Version of Record: A version of this preprint was published at Nature Communications on April 19th, 2022. See the published version at https://doi.org/10.1038/s41467-022-29782-8.

Manufacture-friendly nanostructured metals stabilized by dual-phase honeycomb shell

Hai Wang[1], Wei Song[1,2], Mingfeng Liu[2,3], Shuyuan Zhang[1], Ling Ren[1]*, Dong Qiu[4]*, Xing-Qiu Chen[3], Ke Yang[1]

[1]Shi-changxu Innovation Center for Advanced Materials, Institute of Metal Research, Chinese Academy of Sciences, Shenyang, China.

[2]School of Materials Science and Engineering, University of Science and Technology of China, Shenyang, China

[3]Shenyang National Laboratory for Materials Science, Institute of Metal Research, Chinese Academy of Sciences, Shenyang, China.

[4]Centre for Additive Manufacturing, School of Engineering, RMIT University, Melbourne, Victoria, Australia.

*Correspondence to: Ling Ren, lren@imr.ac.cn. Dong Qiu, dong.qiu2@rmit.edu.au

Abstract

Refining grains to the nanoscale can greatly enhance the strength of metals. But so far the fabrication routes of nanostructured metals are difficult to be applied at a large-scale industrial level owing to their high cost and size limitation. More crucially, the superior properties of nanostructured metals are easily lost during thermoforming process due to their poor microstructural stability, which limits their widespread application in engineering practice. Here we report a facile "Eutectoid element alloying→Quenching→Hot deformation" (*EQD*) strategy, which enables the mass production of a Ti6Al4V5Cu model alloy with α-Ti grain size of 95±32 nm. In addition, rapid co-precipitation of Ti_2Cu and β phases forms a "dual-phase honeycomb shell" (*DPHS*) structure along the grain boundaries and effectively stabilizes the nanosized α-grains. The instability temperature of the nanostructured Ti6Al4V5Cu alloy reaches 973 K ($0.55T_m$). The room temperature tensile strength approaches 1.52±0.03 GPa, which is 60% higher than the Ti6Al4V counterpart without sacrificing its ductility. Furthermore, the tensile elongation at 923 K exceeds 1000%, more than ten times higher than the Ti6Al4V counterpart. Grain growth is not observed even under such an extreme thermal-mechanical coupling condition. This enables nanostructured Ti6Al4V5Cu to be easily shaped to complex components. The aforementioned strategy paves a new pathway to develop manufacture-friendly, high-performance metallic materials and it also has a great potential to be applied in other alloy systems.

Main text

Nanostructured metals (with grain size below 100 nm) exhibit ultrahigh strength and hardness, making them very attractive for developing novel lightweight and energy-efficient structural components.[1-3] However, the large volume fraction of grain boundaries provides a strong driving force for grain coarsening. In most nanostructured metals, prominent grain growth is observed in a temperature range of $0.25\sim0.4T_m$ (T_m is the melting temperature).[4] Under loading conditions, the stability of nanostructured materials is further degraded. For example, in nanostructured pure Al and Ni,[5, 6] mechanically driven grain growth was observed during plastic deformation at room temperature. The inherent thermal and mechanical instability of nanostructured metals render them difficult to be manufactured into bulky components, which severely limit their application in

engineering practice. Consequently, it is a long-term endeavor for material scientists to develop nanostructured metals with higher stability.

Over past few decades, extensive investigations have shown that nanostructures can be stabilized through either thermodynamic or kinetic strategies.[5, 7, 10-15] Thermodynamically, lowering grain boundary energy can reduce the driving force for grain coarsening. This is often achieved by solute segregation, such as in Ni-W, Co-P, and Ni-Fe alloys.[12, 13, 15] In addition, using low angle boundary or twin boundary architectures in pure Cu or Ni can stabilize nanostructures as well.[2, 11, 16] Kinetically, the driving force for grain coarsening could be counteracted by precipitate particles pinning the grain boundaries. This is normally achieved by mechanical alloying, such as in Cu-WC and Cu-Ta alloys.[5, 14] Basing on above theories, the stability of nanostructure can be further enhanced when thermodynamic and kinetic strategies are favorably combined together. However, this requires a more ingenious nanostructured design strategy which should not only employ low-energy interfaces, but also introduce thermally stable secondary phases pinning on the low-energy interfaces.

To achieve this target, we have developed an innovative idea to stabilize nanosized grains by a dual-phase honeycomb shell (*DPHS*) nanostructure (Fig. 1a). Here, equiaxed nanograins are analogous to the compartments in a honeycomb, they are fully encapsulated in thin dual-phase shells. The phases which make up of the dual-phase shells have low interface energy with the matrix. Hence, conventional high angle grain boundaries (HAGBs) with poor thermal stability are replaced by low energy phase boundaries to thermodynamically stabilize the nanostructure. Moreover, the growth of any phase in the dual-phase shell is constrained by the other, thus the shell itself is of high stability. Such stable shells can exert effective pinning force on nanograins to kinetically stabilize the nanostructure when it is exposed to high temperature and/or plastic deformation. We anticipate that such a microstructural design concept that synchronizes the thermodynamics and kinetics strategies would prominently enhance the stability of nanosized grains. To test our hypothesis, we developed a novel Ti6Al4V5Cu alloy as a model alloy in this study.

The microstructural thermal stability of the as-fabricated Ti6Al4V5Cu alloy with an average grain size of 95±32 nm (Supplementary Fig. 1) was determined by exposure for one hour at various temperatures (Fig. 1b). The onset instability temperature, was identified as high as 973 K ($0.55T_m$). This is notably higher than those of the nanostructured metals fabricated through conventional "bottom up" or "top down" technologies at the same grain size level (~100 nm).[4-9] We evaluated the mechanical properties of as-fabricated samples by room temperature tensile tests (Supplementary Fig. 2). The tensile strength is (1.52±0.3) GPa and the elongation is (11±1)%. The comprehensive mechanical properties were greatly improved compared with commercial α, β, or (α+β) titanium alloys in the ASTM standard (Fig. 1c). The phenomenon of strength and ductility trade-off which was often reported in other nano-grained materials did not occur in the present study.[16] This can be attributed to the superior mechanical stability inhibiting the occurrence of strain localization and early necking (Supplementary Fig. 3). Furthermore, we performed high temperature tensile tests at 923 K to examine the stability under a thermal-mechanical coupling condition (Fig. 1d, Supplementary Fig. 3). Surprisingly, the model alloy was not fractured when the elongation exceeded 1000%, meanwhile, the fine grains still remained its initial size after the deformation. This superplasticity and extremely high stability enable this nanostructured material to be easily manufactured complex components through common bulk metal forming processes.

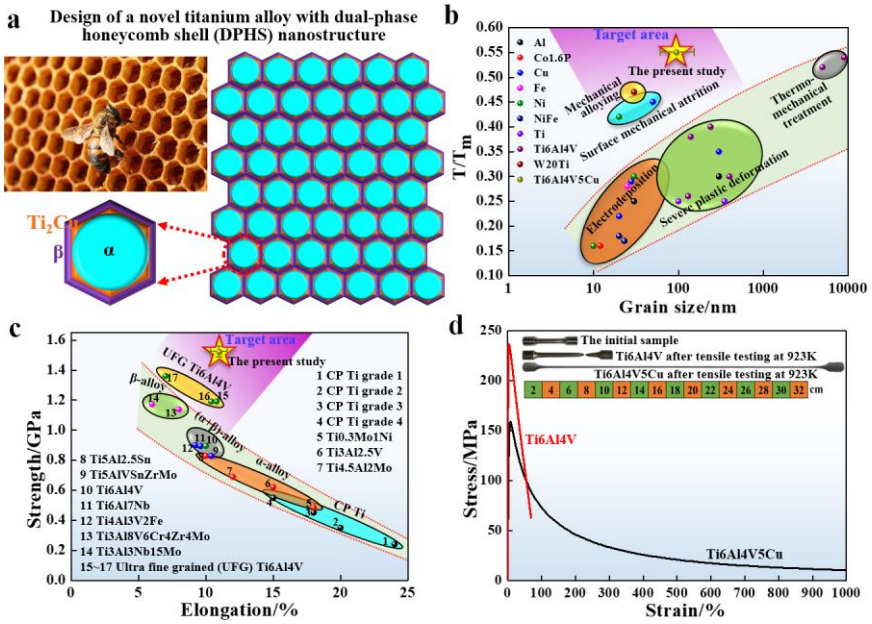

Fig. 1 Design and properties of a novel nanostructured Ti6Al4V5Cu alloy with high stability. **a,** A novel dual-phase honeycomb shell (*DPHS*) nanostructure. **b,** Instability temperature versus average grain size. Literature data for metals processed with electrodeposition,[16] severe plastic deformation,[25-27] thermo-mechanical treatment,[28, 29] surface mechanical attrition,[2,11] and mechanical alloying.[10] **c,** Tensile strength versus elongation. Literature data for titanium alloys in the ASTM standard and ultrafine grained Ti6Al4V alloys.[8, 9] **d,** Strength versus stain curves at 923 K, showing the superplasticity of the Ti6Al4V5Cu alloy.

The superior stability and mechanical properties should be originated from its unique microstructural architecture. Transmission electron microscopy (TEM) analysis performed under the high-angle annular dark field (HAADF) mode indicates that alloying elements segregated along the nano-grain boundaries forming a shell structure (Fig. 2a). We randomly characterized a nano-grain by X-ray energy dispersive spectroscopy (XEDS) analysis (Fig. 2b). The equiaxed, aluminum enriched α-Ti nano-grain is fully enveloped by copper enriched Ti_2Cu phase and vanadium enriched β phase. That is why we call it dual-phase honeycomb shell (*DPHS*) structure.

The formation of nanosized α-Ti grains and *DPHS* structure is credited to our 'Eutectoid element alloying→Quenching→Hot deformation' (*EQD*) strategy (Fig. 2c). Here, the *E* step is to alloy metals with eutectoid-forming elements that will contribute to the formation of eutectoid intermetallics constituting the shell in the last step (*D* step). The *Q* step refers to quenching the material at above the eutectoid transformation temperature. A combination of *E* and *Q* steps strongly suppress the eutectoid reaction, which will generate severe lattice distortion in martensite as a result contributing to the formation of a nano-lathy precursor. The *D* step is to convert the nano-lathy precursor into an equiaxed nano-grained structure through hot deformation. Meanwhile, dual-phase shell formed as a result of strain-assisted phase transformations. The *EQD* process can be achieved by traditional hot processing technologies that are compatible with the present industrial production lines (Supplementary Fig. 4). It well circumvents the dilemma of high-cost and low-efficiency in the current nanostructured metal fabrication strategies.[5, 6, 8, 9] For titanium alloys, eutectoid-forming elements include Cu, Si, Co, Ni, Mn, W, Cr, et. al. Given a high solubility of Cu in β titanium, a big atomic radius difference with respect to titanium, and the fact that Ti_2Cu phase can rapidly

precipitate from α titanium,[17] Cu was short-listed as the alloying element in the most widely used Ti6Al4V alloy in this study.

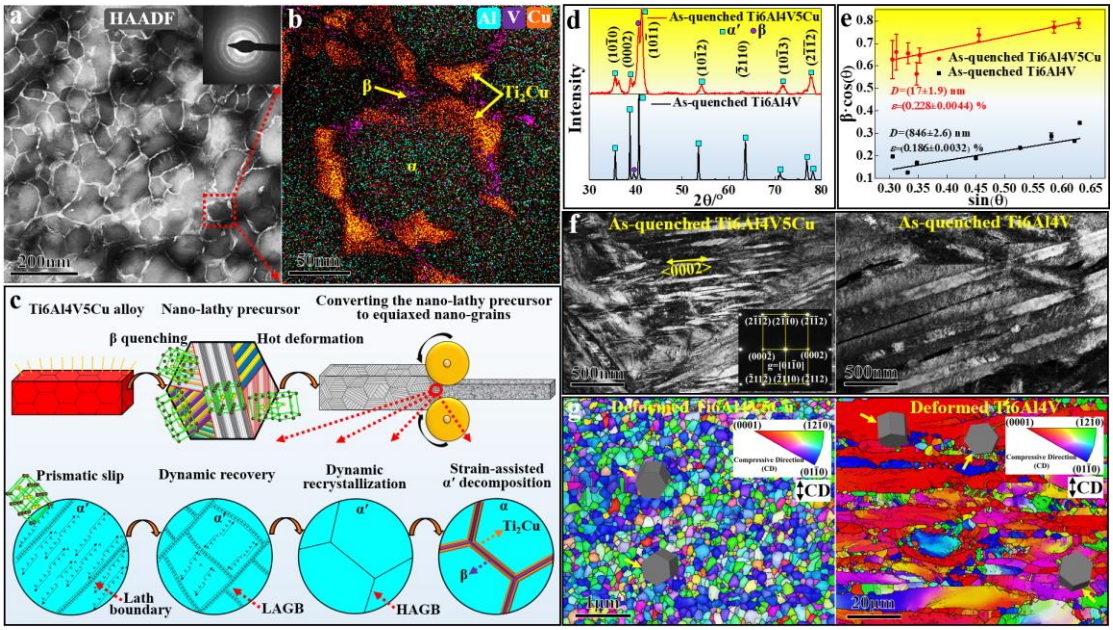

Fig. 2 Microstructure and formation mechanisms. **a,** Transmission electron microscopy (TEM) performing under the high-angle annular dark field (HAADF) mode of the as-prepared Ti6Al4V5Cu alloy. **b,** X-ray energy dispersive spectroscopy (XEDS) analysis. **c,** Schematic shown the eutectoid element alloying, quenching and hot deformation (QD) fabricating strategy. **d,** X-ray diffraction analysis (XRD) of as-quenched materials. **e,** β·cos(θ) versus sin(θ) curves. Lattice strain ε and crystalline domain size D were determined by slopes and intercepts of curves. **f,** TEM bright field images of as-quenched materials. **g,** Inverse pole figures (IPF) of deformed materials.

To determine the formation mechanism of the nano-lathy precursor in *E* and *Q* steps, we performed X-ray diffraction (XRD) analysis on the as-quenched Ti6Al4V5Cu alloy (Fig. 2d). The specimen was mainly identified as α′ phase, hence the eutectoid reaction β→α+Ti_2Cu was substantially inhibited. Given supersaturated copper in the α′ matrix (Supplementary Fig. 5), and large atomic radius difference between titanium (0.147 nm) and copper (0.128 nm), a large lattice strain should be stored in the martensite matrix. This lattice strain is reflected by the significant peak broadening in the XRD spectrum compared to the copper free Ti6Al4V specimen. Further calculation using Williamson-Hall formula indicates that the average lattice strain increases from 0.186% to 0.228% due to copper alloying (Fig. 2e). It is well known that self-accommodation of lattice distortion is achieved by different lathy variants in neighbors.[18] To accommodate the excessive lattice distortion in the copper supersaturated matrix, higher number density of thin lathy variants should be formed. This is consistent with the TEM observation that copper alloying resulted in the lath width significant decreasing from 100~500 nm to 10~70 nm (Fig. 2f).

In order to convert the nano-lathy precursor to an equiaxed nano-grained structure during the *D* step, transversal boundaries that are perpendicular to the longitudinal direction of lath martensite should be introduced. Experimental results showed that all the prismatic planes of hcp α phase are parallel with the longitudinal direction of laths (Fig. 2f, Supplementary Fig. 6). Therefore, only when the prismatic slip is the dominated deformation mode, traversal boundaries can be extensively

generated in the material. This is in agreement with our inverse pole figure (IPF) results (Fig. 2g). In the Ti6Al4V5Cu alloy, a strong prismatic texture which originated from the prismatic slip was characterized, hence traversal boundaries formed and the nano-lathy precursor was successfully converted to an equiaxed nano-grained structure. In the Ti6Al4V alloy, however, an obvious basal texture which originated from the basal slip was observed, this gave rise to the forming of longitudinal boundaries and thus the initial fine laths got coarsened during the deformation. It is generally accepted that the deformation mechanism in hcp metals is either basal or prismatic slip, depending on whether the c/a ratio is above or below 1.60.[19] The XRD measurement indicates that due to copper alloying, the c/a ratio decreased from 1.60 to 1.56 (Fig. 2d), thus explaining why prismatic slip dominated its hot deformation in the Ti6Al4V5Cu alloy.

The newly formed equiaxed α′ nano-grains in the Ti6Al4V5Cu alloy might be with stable low angle grain boundaries (LAGBs) at the beginning of the hot deformation, but they would soon evolve into HAGBs through dynamic recovery and dynamic recrystallization.[19] From the perspective of lowering systematic energy, HAGBs tend to be spontaneously eliminated through grain coarsening.[2] That is why it is very challenging to preserve nanostructure after high temperature deformation. However, in the current model alloy, strain-assisted martensite decomposition $\alpha' \rightarrow \alpha+\beta+Ti_2Cu$ was synchronously triggered by the hot deformation (Supplementary Fig. 7). As the nucleation rate along HAGBs is several orders of magnitude faster than that in the crystal lattice,[20] the conjugated β and Ti_2Cu phase rapidly precipitated at sites of otherwise unstable HAGBs, forming "protective" dual-phase shells enveloping the nano-grains. EBSD observations reveal that these shells did not only inhibit grain coarsening during the high temperature fabrication process, but also significantly enhanced the nanostructured stability against post-fabrication annealing (Fig. 3a). When annealed below 923 K for 1 hour, both the nanostructure and the texture characteristic were barely evolved. That is why the onset thermal instability is determined as 973 K (Fig. 1b).

The outstanding thermal stability we observed supports the belief that nanostructures can be remarkably stabilized when thermodynamic and kinetic strategies were favorable combined together through constructing the *DPHS* structure. Thermodynamically, the driving force for grain coarsening was noticeably reduced when conventional high-energy HAGBs were replaced with low energy α/Ti_2Cu or α/β phase interfaces. By tilting the specimens under high-resolution TEM (Fig. 3b), we found a set of low-lattice-misfit orientation relationships between the core α phase and the shell Ti_2Cu/β phase: $(0001)_\alpha // (013)_{Ti2Cu} // (10\bar{1})_\beta$; $[11\bar{2}0] // [100]_{Ti2Cu} // [111]_\beta$. Based on the first-principles calculations (Fig. 3c), the phase interface energy of α/Ti_2Cu and α/β are only of 0.140 J/m^2 and 0.044 J/m^2 respectively, which are an order of magnitude smaller than that of conventional α/α HAGBs of 0.8~2.0 J/m.[2, 16] This indicates that both phase interfaces enclosing the nanosized α grains are thermodynamically stable. It should be noted that the low energy phase interface in the present study is different from the low energy LAGBs which could gradually accumulate their misorientations at high temperatures to form high energy HAGBs.[21] Our pole figure results (Fig. 3d) proved on a macro level that the initial low-lattice-misfit orientation relationship among α, Ti_2Cu and β phase was still maintained even after annealing at 973 K.

Kinetically, the Ti_2Cu/β dual-phase shells would exert substantial pinning force on α grains hence offsetting the driving force for grain coarsening. Obviously, the role of the Ti_2Cu/β dual-phase shells to a large extent depends on two important factors: Firstly, whether they can precipitate immediately after the formation of nanosized α grains; secondly, the thermal stability of the Ti_2Cu/β shells at elevated temperatures. To elucidate these key issues, we use atom probe tomography (APT) analysis

to provide an insight into the Ti_2Cu/β shells. In the as-fabricated sample (Fig. 3e), there is a prominent copper concentration gradient around the Ti_2Cu phase. This implies that the Ti_2Cu phase was rapidly precipitating from α grains during hot deformation. The average copper concentration in the α phase is (1.4±0.2) at%, thereby, it can be estimated that over 70% of copper atoms have transferred from the matrix to Ti_2Cu phase. We also noticed that vanadium was rejected when Ti_2Cu phase was growing during hot deformation, and this facilitated the nucleation of vanadium enriched β phase around the Ti_2Cu phase. This explains why the Ti_2Cu and β phase are frequently found side-by-side with a conjugated relationship. When the sample was annealed at 923 K for one hour (Fig. 3f), there is no solute copper left in the matrix and this implies that any further coarsening of Ti_2Cu particles will expend other smaller Ti_2Cu particles surrounded. But the presence of adjacent β phase impeded any conceivable mass transfer of copper atoms from surrounding grains. In a similar fashion, the Ti_2Cu phase acted as an effective barrier to hamper the mass transfer of vanadium from grain inside. Consequently, further growth of either phase in the Ti_2Cu/β dual-phase shell is constrained by the other, thus the shell possessed extremely high stability. As a comparison, we have also prepared a nanostructured Ti-5Cu alloy only with Ti_2Cu particles pinning on α grain boundaries (Supplementary Fig. 8). The material presented inferior microstructural stability due to Ti_2Cu particles easily get coarsened at high temperatures.

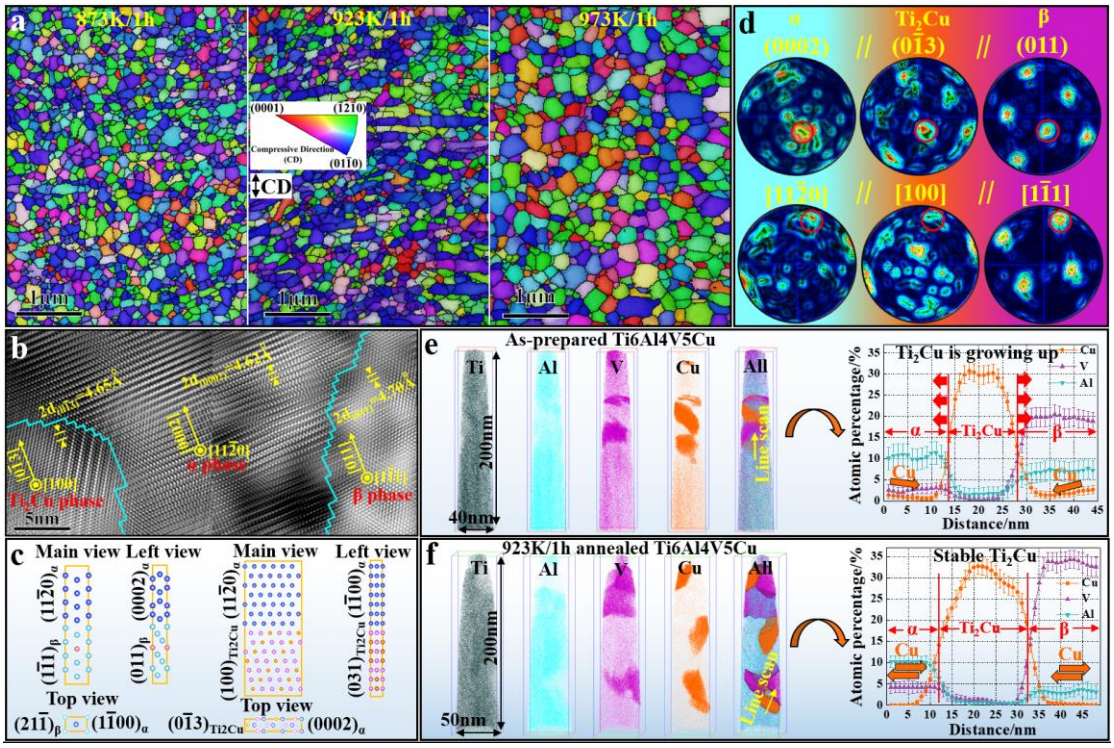

Fig.3 The *DPHS* nanostructure is stabilized thermodynamically and kinetically. **a,** IPF maps of the Ti6Al4V5Cu sample after annealed at various temperatures. **b,** High resolution TEM observation showing a low misfit orientation relationship of α/Ti_2Cu/β phases. **c,** Interfacial structural models for first principles calculations. **d,** Pole figures of the Ti6Al4V5Cu sample after annealed at 973 K, the initial low energy orientation relationship was retained. **e,** Atom probe tomography (APT) analysis in the as-prepared Ti6Al4V5Cu sample, the copper concentration gradient indicating that the Ti_2Cu/β shell can be formed rapidly. **f,** APT analysis of the 923K/1h annealed Ti6Al4V5Cu sample.

More importantly, the Ti_2Cu/β shells can also stabilize the nanostructure under a thermal-mechanical coupling condition, which enabled the material to present outstanding superplasticity at elevated temperatures. In order to understand the mechanism of superplasticity, we performed in-situ scanning electron microscopy observation on a fiducial marked sample prepared by focused ion beam milling (Fig. 4a, 4b). After loading at 923 K to an average tensile strain of 40%, we neither observed any dislocation slip band, nor change in grain size or aspect ratio (Fig. 4c). This precluded the occurring of conventional deformation mechanisms such as dislocation slip or Coble diffusional creep in coarse grained materials.[22] The fiducial markers were bent or even broken off at phase interfaces, demonstrating that phase interface sliding took place (Fig. 4d). We calculated the strain distribution in the material by measuring the displacement of the fiducial markers (Fig. 4e). Regions with larger strains always corresponded to the place where significant phase interface slip occurred, therefore, the superplastic deformation should be governed by phase boundary sliding (Fig. 4f). Although superplasticity phenomenon has ever been reported in other nano-grained metals,[23] it should be noted that the dominated deformation mechanisms in those studies were grain boundary migration and grain growth. As fine grains cannot be retained after the superplastic deformation, mechanical properties of the initial nanostructure would inevitably be reduced.

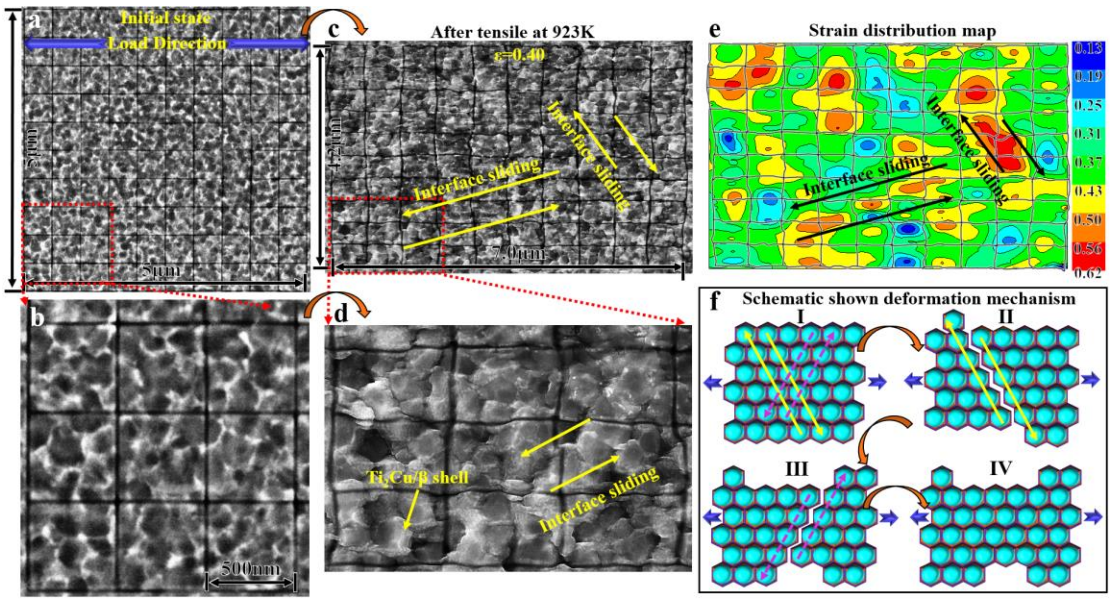

Fig. 4 In-situ scanning electron microscopy (SEM) observation performing on a fiducial marked sample in the 923 K tensile test. **a, b,** SEM images of the sample before tensile test, shells of α grains can be viewed. **c, d,** SEM images of the sample after tensile to the strain of 0.4, the bending of fiducial markers denotes phase interface sliding taking place. **e,** A strain distribution map, regions with larger strains correspond to where significant phase interface slip happens. **f,** Schematic shown of the superplastic mechanism in the alloy.

In this study, we have demonstrated a pathway to achieve ultra-stable nanosized grains by constructing a *DPHS* nanostructure through a low-cost *EQD* strategy in a Ti6Al4V5Cu model alloy. As a result, the key challenge to retain nanosized grains in metal bulk forming processes has been effectively overcome. Moreover, the *EQD* strategy is also applicable in other eutectoid alloy systems when a martensitic transformation is available. For example, we have also fabricated high stability

Ti15Zr7Cu alloy with a *DPHS* nanostructure (Supplementary Fig. 9, 10). We expect that the strategy reported here can be extended to other alloy systems, such as alloy steels, promoting the development and mass applications of bulky nanostructured metal products in future.

Methods

Materials

For preparing the Ti6Al4V5Cu alloy, Ti, Al, V, Cu raw materials were consolidated to bulks through an anvil apparatus in which three orthogonal pistons compressed a cuboid chamber. Cuboid billets with the size of 180×180×450 mm were prepared then welded together forming a long billet. They were melted by vacuum consumable furnace to a 700 kg big ingot with the diameter of 380 mm. The ingot was hot forged at above 1173 K into bars with the diameter of (60±2) mm and length of (1.5±0.3) m. After hot forging, the bars were immediately quenched to room temperature in 30 wt.% NaCl water solution. Cylindrical samples with 60 mm in diameter and 140 mm in height were sectioned from the as-quenched rolling bars. They were isothermally compressed at 1013 K by hydraulic press to a height of 15 mm under a compressive strain rate of 2 s^{-1}. The as-prepared Ti6Al4V5Cu material were plates with the diameter of (175±10) mm. The upper and lower edges of the plate were removed with grinding machines by 2mm.

For preparing Ti6Al4V, Ti5Cu and Ti15Zr7Cu alloys, their raw materials were consolidated to bulks through the anvil apparatus. Billets were melted using a 20 kg vacuum consumable furnace. The as-melted ingots were hot forged at above 1173 K into bars with the diameter of 60 mm and length of (0.8±0.2) m, then immediately quenched to room temperature in a 30 wt.% NaCl water solution. Next, Ti6Al4V, Ti5Cu, and Ti15Zr7Cu alloys were compressed at 1013 K, 1033 K, and 983 K, respectively. Details of their fabricating procedures were the same as aforementioned Ti6Al4V5Cu alloy. Chemical compositions (wt.%) of materials being studied were displayed in Supplementary Table1.

Tensile testing

Tensile tests were performed on a Shimadzu AG-100KN universal testing machine which was equipped with a non-contact laser extensometer. Standard cylinder samples with the diameter of 5 mm and gauge length of 25 mm (ASTM standard E8/E8M-08) were used. They were machined with the use of the as-prepared Ti6Al4V5Cu plates. Tensile loading direction was perpendicular to the thickness direction of Ti6Al4V5Cu plates. Room temperature tensile tests were conducted with an initial strain rale of 0.001 s^{-1}. High temperature tensile tests were conducted at 923 K with an initial strain rale of 0.01 s^{-1}. The strength and elongation of samples were given by the averages of five parallel measurements.

X-ray diffraction (XRD) analysis

Samples for XRD analysis were mechanically polished, then electrolytic polished by a mix solution of 5 vol.% perchloric acid, 35 vol.% n-butyl alcohol and 60 vol.% methanol at 25 V for 20 s. XRD experiments were performed on a Bruker D8 X-ray diffractometer using a Cu anode, the diffraction angular is in a range of 30° to 180°with a step size of 0.02°and a counting time of 5 s. The reflections of $\{10\bar{1}0\}$, $\{0002\}$, $\{10\bar{1}1\}$, $\{10\bar{1}2\}$, $\{2\bar{1}10\}$, $\{10\bar{1}3\}$ and $\{2\bar{1}\bar{1}2\}$ of the α′ phase were measured. The modified Williamson-Hall formula was used to calculate the lattice strain ε and crystalline domain size D[24]:

$$\beta \cdot \cos(\theta) = \frac{\lambda}{D} + 5\sin(\theta)\varepsilon \tag{1}$$

where, β is the integral peak width, θ is the diffraction angle, λ=0.15418 nm is the X-ray wavelength.

Electron backscattered diffraction (EBSD) analysis

Samples for EBSD analysis were sectioned along the compression direction by wire-electrode cutting, then mechanically grinded and polished, finally subjected to vibration polished using a VibroMet2 machine in the nano silica polishing slurry for 24 h. The scanning step size of samples was 0.02 μm. Acquired data was analyzed by HKL-Channel 5 software. The color code in the inverse pole figure (IPF), blue for $<10\bar{1}0>_{\alpha}$, red for $<0001>_{\alpha}$, and green for $<11\bar{2}0>_{\alpha}$, gives the crystallographic orientation of each grain pointing in the direction parallel to the compressive direction (CD). Boundaries with misorientations larger than 15° were defined as high angle boundaries (HAGBs), they were labeled in bold line. While boundaries with misorientations between 2~15° were defined as low angle grain boundaries (LAGBs), they were labeled in thin line. Pole figures of $<0001>_{\alpha}$, $<11\bar{2}0>_{\alpha}$, $<013>_{Ti2Cu}$, $<100>_{Ti2Cu}$, $<10\bar{1}>_{\beta}$, $<111>_{\beta}$ were used to analyze the crystallographic orientation relationship between α, Ti_2Cu and β phase.

Transmission electron microscopy (TEM) observation

Samples for TEM observation were ground to a thickness of below 40 μm. Foils with a diameter of 3 mm were punched out and two-jet thinning in an electrolyte of 5 vol.% perchloric acid, 35 vol.% n-butyl alcohol and 60 vol.% methanol at -30°C by a voltage of 25 V, followed by ion-beam thinning at 2 keV using a Gatan PIPS^{TM} facility. TEM observations were performed on a JEOL 2100 F microscope which was equipped with a X-ray energy dispersion spectrum detector and operated at 200 kV. High-angle annular dark field (HAADF) mode were used to characterize the *DPHS* nanostructure. X-ray energy dispersive spectroscopy (XEDS) analysis were used to reveal the chemical composition distribution in the shell structure. High resolution TEM mode were used to identify α, Ti_2Cu and β phase and to determine their crystallographic orientation relationship.

Atom probe tomography (APT) analysis

Samples for APT analysis were fabricated using a dual-beam focused ion beam (FIB) on Helios Nanolab 600i from FEI. Rectangular cubes with dimensions of 2×2×10 μm were extracted from samples' surface then mounted on silicon microtips. Following, they were trimmed by annular ion milling to sharp needles with tip diameter of 30~60 nm and length of 6 μm. APT experiments were performed on a LEAP 4000X instrument, at a sample chamber temperature of 50 K, under a pulse frequency of 200 kHZ and a target evaporation rate of 0.8% per pulse. APT Data reconstruction were analyzed by Cameca IVAS 3.6 software.

In-situ tensile scanning electron microscopy (SEM) observation

The specimen for the in-situ tensile test was a plate with gauge portion dimensions of 2 mm length×3 mm width ×1 mm thick, it was sectioned from the central part of the as-prepared Ti6Al4V5Cu plate. The surface was electropolished by a mix solution of 10 vol.% perchloric acid and 90 vol.% alcohol at -30°C by a voltage of 25 V. In order to measure the strain distribution in the specimen, fiducial markers were drawn on the surface by the FIB instrument. Markers were carved as light as possible to avoid cutting the sample. Dimensions of the fiducial markers was 5×5 μm with pitches of 500 nm. The in-situ tensile experiment was performed on a micro-tensile testing stage, placed inside the chamber of a TESCAN MIRA high resolution scanning electron microscope. The module is equipped with a resistance heater, which is capable of heating up to 1123 K. The temperature of the specimen was precisely controlled by a thermocouple wire spot welded on the sample surface. The tensile test was conducted at 923 K at a strain rate of $0.01s^{-1}$. Every 10% of strain increment the tensile test was paused to acquire a SEM image.

First-principles calculations of phase interface energies

In order to calculate α/β and α/Ti_2Cu phase interface energies, we have constructed interfacial structural models basing on the experimental orientation relationship of $(0002)_\alpha//(0\bar{1}3)_{Ti2Cu}//(011)_\beta$ and $[11\bar{2}0]_\alpha//[100]_{Ti2Cu}//[1\bar{1}1]_\beta$(Fig. 3c). In terms of interface model consisting of two phases M and N, the interfacial energy can be expressed as:

$$\gamma = \frac{E_{sys} - mE_M^{bulk} - nE_N^{bulk}}{A} - \sigma_M - \sigma_N \quad (2)$$

where E_{sys} is the total energy of the interfacial modeling system, E_M^{bulk} and E_N^{bulk} are the energies in bulk M or N system in the unit of eV/atom, A is the surface area of the interfacial structure, m and n are the number of atoms in the slabs of M and N. Here, $\sigma_M$and σ_N are the surface energy of the slab of M and N, which can be derived through the following equation as:

$$\sigma = \frac{1}{2A}(E_{slab} - nE_{bulk}) \quad (3)$$

where E_{slab} is the total energy of the relaxed slab, E_{bulk} is the total energy of the bulk per atom, A is the surface area of the slab. We have constructed surface models in which two topmost atomic layers are allowed to be relaxed to simulate the free surface and the other layers are fixed to describe bulk phase. A 15Å vacuum is used for the models to minimize the interaction in periodic images.

By means of the first-principles calculation within the framework of the Density Functional Theory, we have calculated all above energies by employing the Vienna ab initio simulation package (VASP). We have adopted the projected augmented wave (PAW) method in describing the plane-wave basis and the generalized gradient approximation (GGA) of the Perdew-Burke-Ernzerhof (PBE) in describing the exchange-correlation functional. The valence electrons of Ti, Cu and V atoms are treated as $3p^6 3d^2 4s^2$, $3d^{10} 4s^1$ and $3p^6 3d^3 4s^2$. The cut-off energy of the plane waves is set at 400 eV. All the Brillouin zone integrations are performed on the Gamma centered *k*-mesh and sampled with a resolution of $2\pi \times 0.025$ Å^{-1}.

Data availability

The data that support the findings of this study are available on request from the corresponding author.

References

1 Lu, L., Chen, X., Huang, X. & Lu, K. Revealing the Maximum Strength in Nanotwinned Copper. *Science* **323**, 607 (2009).

2 Liu, X. C., Zhang, H. W. & Lu, K. Strain-Induced Ultrahard and Ultrastable Nanolaminated Structure in Nickel. *Science* **342**, 337 (2013).

3 Liddicoat, P. V. et al. Nanostructural hierarchy increases the strength of aluminium alloys. *Nat. Commun.* **1**, 63 (2010).

4 Shan, Z. et al. Grain boundary-mediated plasticity in nanocrystalline nickel. *Science* **305**, 654-657 (2004).

5 Darling, K. et al. Extreme creep resistance in a microstructurally stable nanocrystalline alloy. *Nature* **537**, 378 (2016).

6 Hu, J., Shi, Y. N., Sauvage, X., Sha, G. & Lu, K. Grain boundary stability governs hardening and softening in extremely fine nanograined metals. *Science* **355**, 1292 (2017).

7 Zheng, S. et al. High-strength and thermally stable bulk nanolayered composites due to twin-induced interfaces. *Nat. Commun.* **4**, 1696 (2013).

8 Semenova, I. P. et al. Fracture toughness at cryogenic temperatures of ultrafine-grained Ti-6Al-4V alloy processed by ECAP. *Mat. Sci. Eng. A* **716**, 260-267 (2018).

9 Zhang, Z. X., Qu, S. J., Feng, A. H. & Shen, J. Achieving grain refinement and enhanced mechanical properties in Ti-6Al-4V alloy produced by multidirectional isothermal forging. *Mat. Sci. Eng. A* **692**, 127-138 (2017).
10 Chookajorn, T., Murdoch, H. A. & Schuh, C. A. Design of Stable Nanocrystalline Alloys. *Science* **337**, 951 (2012).
11 Zhou, X., Li, X. Y. & Lu, K. Enhanced thermal stability of nanograined metals below a critical grain size. *Science* **360**, 526-530 (2018).
12 Weertman, J. R. Retaining the Nano in Nanocrystalline Alloys. *Science* **337**, 921 (2012).
13 Fan, G. J., Fu, L. F., Choo, H., Liaw, P. K. & Browning, N. D. Uniaxial tensile plastic deformation and grain growth of bulk nanocrystalline alloys. *Acta Mater.* **54**, 4781-4792 (2006).
14 Cao, C. et al. Bulk ultrafine grained/nanocrystalline metals via slow cooling. *Sci. Adv.* **5**, 2398 (2019).
15 Li, L. et al. Simultaneous reductions of dislocation and twin densities with grain growth during cold rolling in a nanocrystalline Ni-Fe alloy. *Scr. Mater.* **60**, 317-320 (2009).
16 Lu, K. Stabilizing nanostructures in metals using grain and twin boundary architectures. *Nat. Rev. Mater.* **1**, 16019 (2016).
17 Zhang, D. et al. Additive manufacturing of ultrafine-grained high-strength titanium alloys. *Nature* **576**, 91-95 (2019).
18 Furuhara, T., Kawata, H., Morito, S. & Maki, T. Crystallography of upper bainite in Fe-Ni-C alloys. *Mat. Sci. Eng. A* **431**, 228-236 (2006).
19 Cao, Y., Ni, S., Liao, X., Song, M. & Zhu, Y. Structural evolutions of metallic materials processed by severe plastic deformation. *Mat. Sci. Eng. R* **133**, 1-59 (2018).
20 Inoue, A., Nitta, H. & Iijima, Y. Grain boundary self-diffusion in high purity iron. *Acta Mater.* **55**, 5910-5916 (2007).
21 Gourdet, S. & Montheillet, F. A model of continuous dynamic recrystallization. *Acta Mater.* **51**, 2685-2699 (2003).
22 Kassner, M. E. *Fundamentals of creep in metals and alloys.* (Butterworth-Heinemann 2015).
23 McFadden, S., Mishra, R. S., Valiev, R., Zhilyaev, A. & Mukherjee, A. Low-temperature superplasticity in nanostructured nickel and metal alloys. Nature, 398, 684 (1999).
24 Williamson, G. K. & Hall, W. H. X-ray line broadening from filed aluminium and wolfram. *Acta Mater.* **1**, 22-31 (1953).
25 Zherebtsov, S. V., Kudryavtsev, E. A., Salishchev, G. A., Straumal, B. B. & Semiatin, S. L. Microstructure evolution and mechanical behavior of ultrafine Ti6Al4V during low-temperature superplastic deformation. *Acta Mater.* **121**, 152-163 (2016).
26 Stolyarov, V. V., Zhu, Y. T., Alexandrov, I. V., Lowe, T. C. & Valiev, R. Z. Grain refinement and properties of pure Ti processed by warm ECAP and cold rolling. *Mat. Sci. Eng. A* **343**, 43-50 (2003).
27 Wang, Y., Chen, M., Zhou, F. & Ma, E. High tensile ductility in a nanostructured metal. *Nature*, **419**, 912 (2002).
28 Zherebtsov, S., Murzinova, M., Salishchev, G. & Semiatin, S. L. Spheroidization of the lamellar microstructure in Ti-6Al-4V alloy during warm deformation and annealing. *Acta Mater.* **59**, 4138-4150 (2011).
29 Chao, Q., Hodgson, P. D. & Beladi, H. Thermal stability of an ultrafine grained Ti-6Al-4V alloy during post-deformation annealing. *Mat. Sci. Eng. A* **694**, 13-23 (2017).

Acknowledgements

This work was financially supported by the National Key Research and Development Program of China (2018YFC1106600, 2016YFC1100600), LiaoNing Revitalization Talents Program (XLYC1807069), National Natural Science Foundation (No. 51631009, 31870954, 51725103). Doctoral Scientific Research Foundation of LiaoNing Province (2020BS002).

Author contributions

Hai Wang and Ren Ling developed the concept, designed the experiments. Dong Qiu and Xingqiu Chen gave guidance on experimental design and writing. Ling Ren and Ke Yang supervised the project. Hai Wang, Wei Song and Shuyuan Zhang prepared the samples, characterized structures and measured properties. Mingfeng Liu and Xing-Qiu Chen performed modeling and simulation. Hai Wang, Dong Qiu and Ling Ren wrote the paper.

Competing interests

Authors declare no competing interests.

Supplementary data

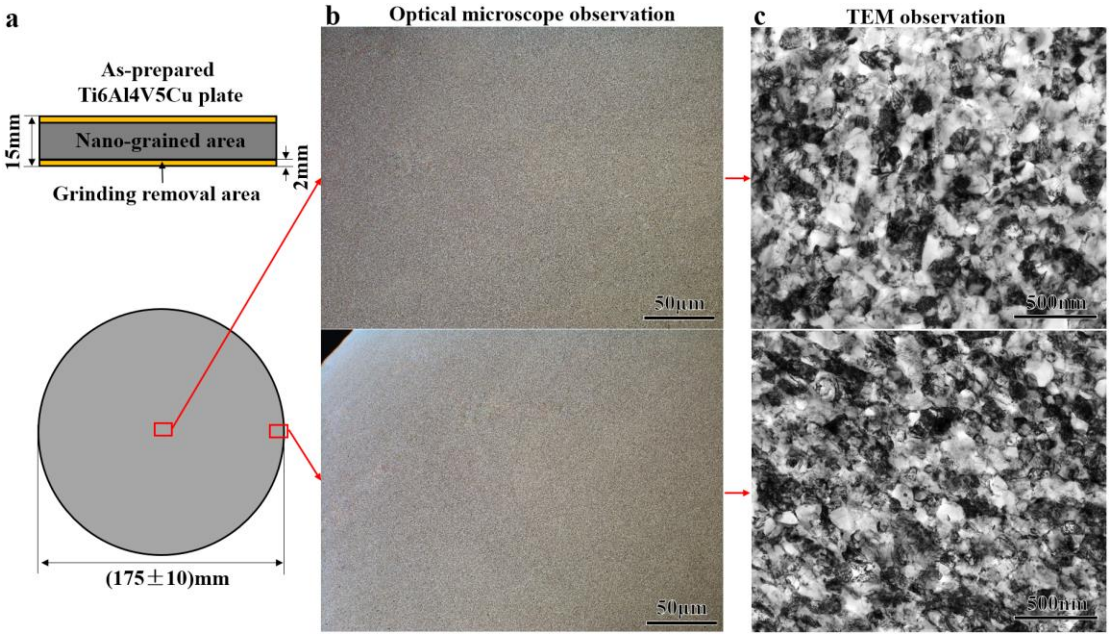

Supplementary Fig. 1 As-prepared nanostructured Ti6Al4V5Cu alloy. **a,** Schematic diagrams showing the dimensions of the plate. **b,** Optical microscope observations showing a homogenously distributed ultra-fine microstructure. **c,** TEM observations revealing an equiaxed nano-grained structure.

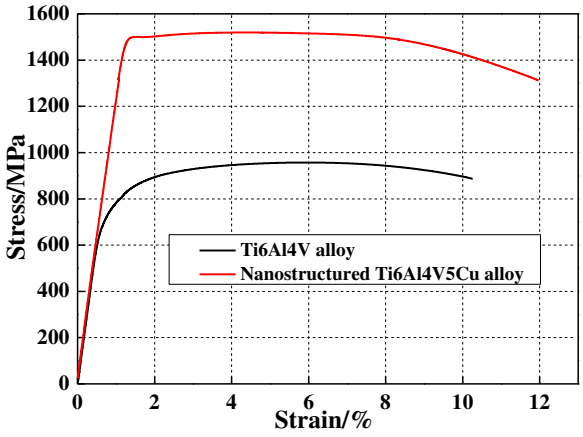

Supplementary Fig. 2 Tensile curves of the as-prepared Ti6Al4V5Cu and Ti6Al4V alloy.

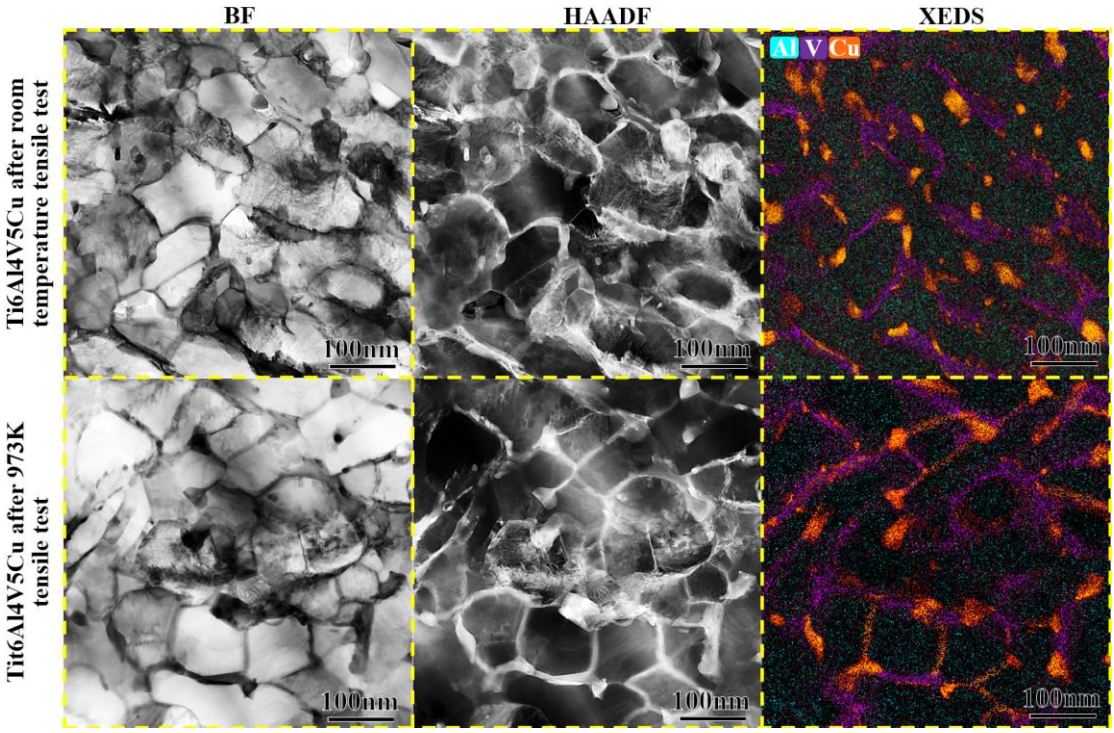

Supplementary Fig. 3 TEM observation of the nanostructured Ti6Al4V5Cu alloy. Images were taken under bright field (BF), high angle annular dark field (HAADF), and X-ray energy dispersive spectroscopy (XEDS) mode. The nanostructure was barely evolved after room and high temperature tensile tests, indicating the material possessed excellent mechanical and thermal-mechanical coupling stability.

Supplementary Fig. 4 Fabrication procedures for the nanostructured Ti6Al4V5Cu alloy

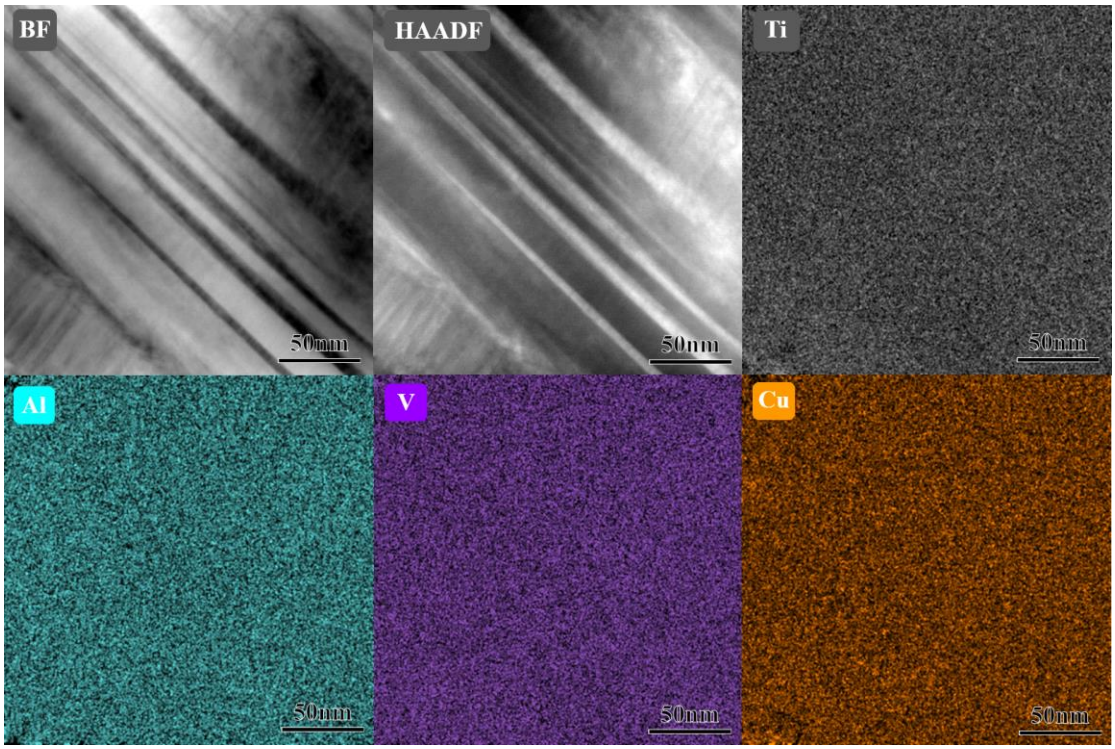

Supplementary Fig. 5 TEM observation of the as-quenched Ti6Al4V5Cu alloy. XEDS maps show that elements are homogenously distributed in the material.

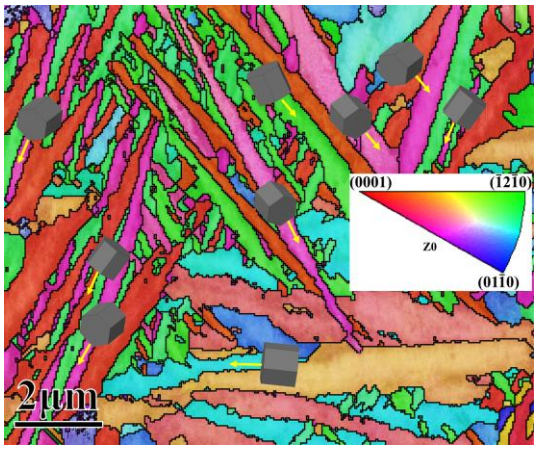

Supplementary Fig. 6 IPF maps of as-quenched Ti6Al4V5Cu alloy. All the prismatic planes of hcp α phase are parallel with the longitudinal direction of laths.

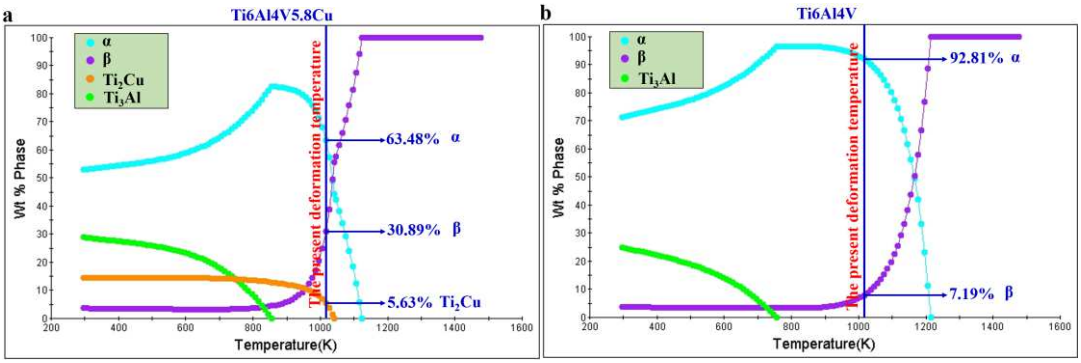

Supplementary Fig. 7 Equilibrium phase diagram calculated by JMatPro software. **a,** Ti6Al4V5Cu alloy. **b,** Ti6Al4V alloy.

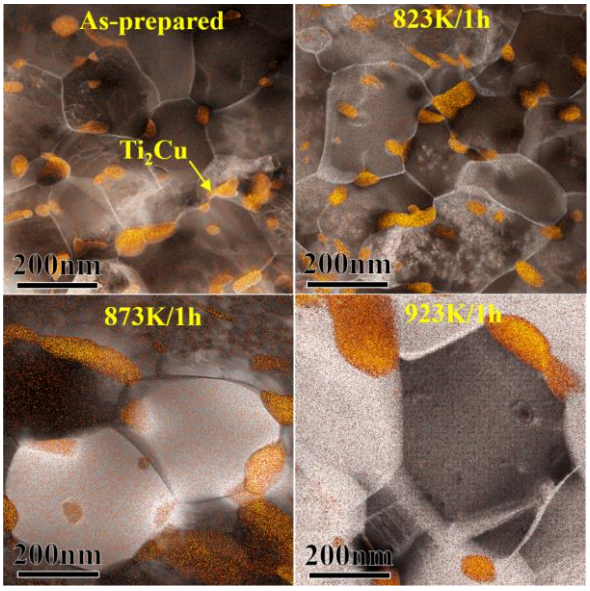

Supplementary Fig. 8 Thermal stability against annealing of the nanostructured Ti5Cu alloy. It showed inferior stability against annealing than the Ti6Al4V5Cu alloy with *DPHS* nanostructure.

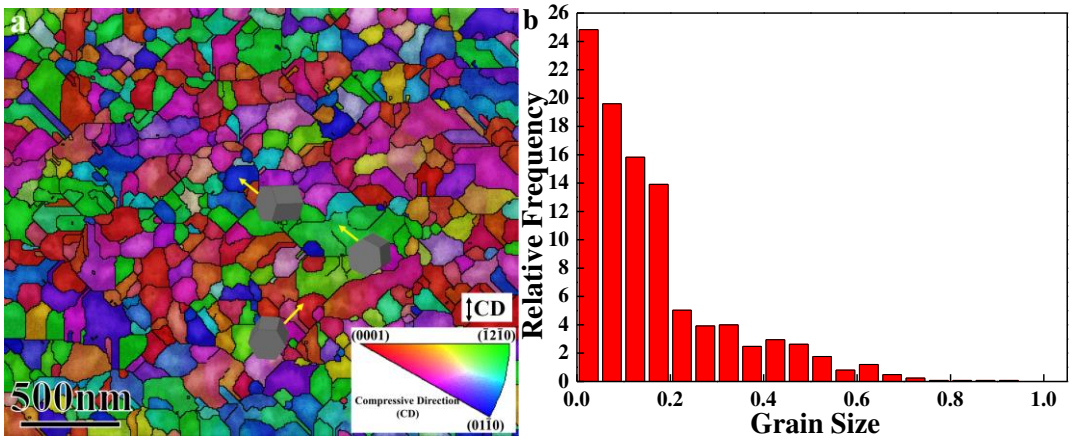

Supplementary Fig. 9 EBSD analysis of the as-prepared Ti15Zr7Cu alloy. **a,** The IPF image showing that an ultrafine-grained structure have been fabricated following the QD strategy. **b,** Grain size distribution map. Over 44% of grains are with sizes below 100 nm

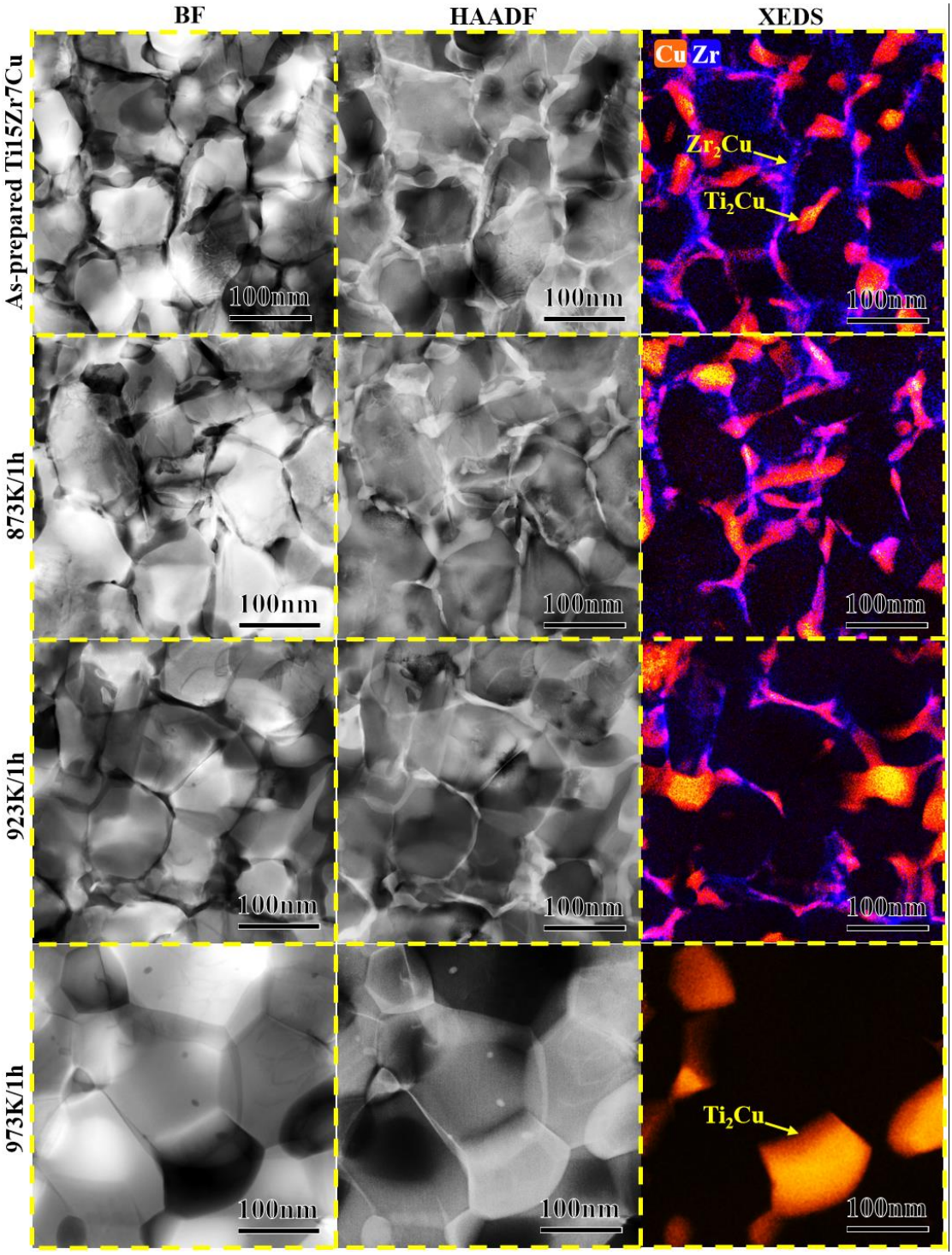

Supplementary Fig. 10 TEM observation of the Ti15Zr7Cu alloy. A *DPHS* nanostructure has been successfully fabricated following the QD strategy, the dual-phase shell was composed of Ti_2Cu and Zr_2Cu phase. The nanostructured alloy presents extreme high stability against annealing, the onset of grain coarsening temperature is up to 973K.

Supplementary Table1 Chemical compositions (wt.%) of alloys being investigated

	Al	V	Cu	Zr	Fe	O	C	Ti
Ti6Al4V5Cu	6.2	4.0	5.8	—	0.02	0.04	0.02	Bal.
Ti6Al4V	6.1	3.9	＜0.01	—	0.07	0.09	0.03	Bal.
Ti5Cu	—	—	5.1	—	0.03	0.07	0.02	Bal.
Ti15Zr7Cu	—	—	7.0	14.8	0.03	0.02	0.01	Bal.